HHS Public Access

Author manuscript

Adv Mater. Author manuscript; available in PMC 2024 January 01.

Published in final edited form as:

Adv Mater. 2023 January ; 35(3): e2206385. doi:10.1002/adma.202206385.

3D-bioprinted phantom with human skin phototypes for biomedical optics

Wonjun Yim[1], **Jiajing Zhou**[2], **Lekshmi Sasi**[2], **Jiayu Zhao**[2], **Justin Yeung**[4], **Yong Cheng**[2], **Zhicheng Jin**[2], **Wade Johnson**[2], **Ming Xu**[2], **Jorge Palma-Chavez**[2], **Lei Fu**[2], **Baiyan Qi**[1], **Maurice Retout**[2], **Nisarg J. Shah**[2,3], **Jinhye Bae**[1,2,3], **Jesse V. Jokerst**[1,2,3,5,*]

[1]Materials Science and Engineering Program, University of California San Diego, La Jolla, CA, USA

[2]Department of Nanoengineering, University of California San Diego, La Jolla, CA, USA

[3]Chemical Engineering Program, University of California San Diego, La Jolla, CA, USA

[4]Department of Bioengineering, University of California San Diego, La Jolla, CA, USA

[5]Department of Radiology, University of California San Diego, La Jolla, CA, USA

Abstract

We report 3D-bioprinted skin-mimicking phantoms with skin colors ranging across the Fitzpatrick scale. These tools can help understand the impact of skin phototypes on biomedical optics. Synthetic melanin nanoparticles of different sizes (70–500 nm) and clusters were fabricated to mimic the optical behavior of melanosome. The absorption coefficient and reduced scattering coefficient of the phantoms are comparable to real human skin. We further validated the melanin content and distribution in the phantoms *versus* real human skins *via* photoacoustic (PA) imaging. The PA signal of the phantom could be improved by (i) increasing melanin size (3–450-fold), (ii) increasing clustering (2–10.5-fold), and (iii) increasing concentration (1.3–8-fold). We then used multiple biomedical optics tools (*e.g.,* PA, fluorescence imaging and photothermal therapy) to understand the impact of skin tone on these modalities. These well-defined 3D-bioprinted phantoms may have value in translating biomedical optics and reducing racial bias.

Graphical Abstract

*Correspondence and requests for materials should be addressed to J.V.J. (jjokerst@eng.ucsd.edu).

Author contributions.

W.Y. and J.V.J. conceived the idea and designed the materials and method for skin phototypes-mimicked phantoms. W.Y. conducted the major material synthesis and experimental works. J.Z., L.S., J.Z., and J.B. helped with 3D-bioprinting experiments. J.Y., Y.C., Z.J., M.X., L.F., B.Q., and M.R. assisted with material design & characterizations. W.J. and N.J.S. helped with fluorescence experiments. W.Y. and J.V.J. analyzed the result and wrote the manuscript with inputs from all authors.

The authors declare no competing financial interest

Code availability

A custom code (adding-doubling algorithm) is available for research purposes from the corresponding author upon requests.

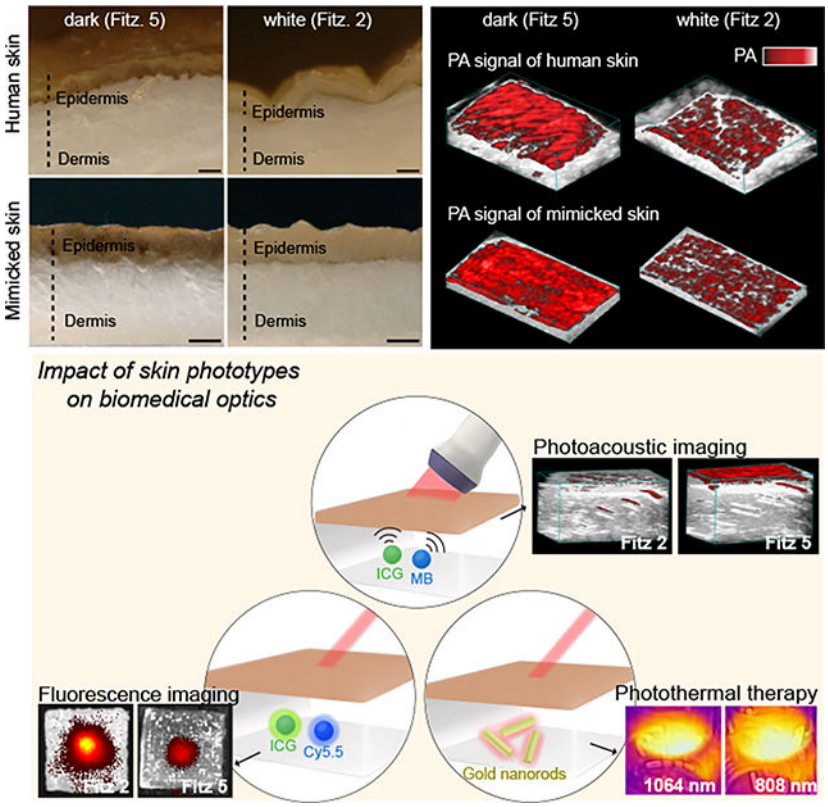

The authors report skin-mimicking phantoms with different Fitzpatrick scale values to understand the impact of skin phototypes on biomedical optics. The absorption and scattering coefficients of the skin phantoms were similar to real human skin. This approach may have value in understanding differences in the performance of biomedical optics as a function of skin tone.

Keywords

3D-bioprinting; bioinspired materials; artificial skin; biophotonic devices

Introduction

Human skin offers important physical and immunological protection. It protects against injury, shields radiation, and offers antioxidant defense.[1,2] Skin consists of a lamellar structure with diverse cell types (*e.g.,* immune cells, melanocytes, and basal cells) that periodically detach from the basement membrane, move to the surface, and die for self-renewal.[3] Melanocytes are a critical cell type that generate melanin to absorb ultraviolet (UV) light (290–400 nm), which is a major risk for skin diseases (*e.g.,* melanoma) due to DNA damage.[4–7] Here, melanin-containing organelles called melanosomes are transferred to the surrounding keratinocytes. This increase in melanosome concentration leads to darker skin phototypes, and darker phototypes can be a function of racial background or previous sun exposure, *i.e.,* tanning.[8] Indeed, skin pigmentation depends on variations in the size, number, clustering phase, and the proportions between melanin species (*e.g.,* eumelanin and pheomelanin).[9] Skin pigmentation has been quantified using melanosome volume fraction

(M_f) parameter: 1.3–6.3% for lightly pigmented adults, 11–16% for moderately pigmented adults, and 18–43% for darkly pigmented adults.[10]

Variations in skin phototypes can complicate biomedical optics. Melanin absorption increases linearly from 800 to 600 nm and exponentially from 600 to 300 nm.[11,12] Darker skin phototypes can absorb and scatter more photons: As a result, incident light is attenuated before it reaches the target of interest, and signal transmission can be impeded back to the sensor. Therefore, variations in skin phototypes have negatively affected many forms of medical optic technology including pulse oximetry,[13,14] cerebral tissue oximeters,[15] optical coherence tomography,[16] wearable electronics,[17–19] photoacoustic imaging,[20] fluorescence imaging,[21] and photothermal therapy.[22] One recent study compared 48,097 pairs of oxygen saturation levels measured by pulse oximetry and arterial blood gas test obtained from 8,675 White patients and 1,326 Black patients.[13] The results found that pulse oximetry had trouble in diagnosing hypoxemia in 11% Black patients and 3% White patients due to light absorption by melanin.[13,14] Furthermore, wearable electronics (*e.g.,* smartwatches) have reported inaccuracies in heart rate readings occurring more often in users with dark skin than light skin.[17,18] Clearly, the impact of differences in skin phototypes underscore the ongoing need to understand and correct racial bias in optical technologies. While larger cohort studies are ideal to define and rectify such bias, tissue-mimicking phantoms that recreate the optical properties of human skin as a function of skin phototypes could offer dramatic time- and cost savings.[23,24] These phantoms would be attractive to regulatory agencies, device development firms, and patients.

Here, we engineered 3D-bioprinted phantoms with skin phototypes containing synthetic melanin with controllable particle sizes and clustering to mimic the epidermis of different skin phototypes ranging from Fitzpatrick (Fitz) scale 1 to 6.[23,25] The photoacoustic (PA) signal of human skin changes as a function of melanin absorption:[26,27] The light absorbed by melanin is converted to spatially-confined heat that generates acoustic waves.[28–30] This implies that PA can indirectly measure melanosome content and distribution in human skin. Fitz. 5 human cadaver skin showed 3.5-fold higher PA signal than Fitz. 2 human cadaver skin due to higher melanosome content (Figure 1a and Figure S1).

To mimic variable melanosomes in human skin, we studied optical properties and PA signal of synthetic melanin (*i.e.,* polydopamine) over (i) different sizes (ii) mixtures of different sized particles, and (iii) clustering phases which are biologically relevant to real melanosomes.[31] Gelatin methacrylate (GelMA)—biomacromolecule gelatin obtained from denatured collagen—was used as a bio-ink (*i.e.,* matrix).[32] 3D bioprinting was then used to fabricate a customized GelMA-based phantom with a thin melanin-containing layer (*i.e.,* mimicking the epidermal layer in human skin) (Figure 1b). Finally, we quantitatively examined the impact of skin phototypes on PA imaging, fluorescence imaging, and photothermal imaging at different wavelengths (*e.g.,* 680, 800, and 1064 nm) (Figure 1c). Our skin-tone phantom built up by 3D bioprinting is expected to serve as a benchmark calibration tool of light-mediated diagnostics toward clinical use and further underpin development of biomedical optics.

Results and discussion

Design of synthetic melanin.

Melanin biogenesis occurs through an oxidation process of tyrosine to dopaquinone by tyrosinase.[33] Melanosomes in human skin vary in terms of size (100 nm up to 500 nm), shape (*e.g.,* spherical or elliptical), and number of clusters (Figure 2a).[9,31] Although the overall structure of melanin remains unclear, the basic structural unit of melanin is a mixed polymer predominantly containing indoles.[33] Melanin from human skin or hair is challenging to obtain because it requires harsh extraction conditions (*e.g.,* strong acids or bases) and multiple purification steps.[34] Thus, polydopamine (PDA) was employed here because of its similarity to real melanin in optical absorption, chemical composition, and structure.[35,36] Dopamine can be oxidized into dopamine quinone under basic conditions and further self-polymerize into indole-rich PDA:[37,38] This structure is widely considered to be a synthetic melanin[36] (Figure 2b). To mimic the variable sizes of melanosomes, we synthesized spherical PDA nanoparticles with different diameters of 70, 120, 300, and 500 nm (referred to as PDA_{70}, PDA_{120}, PDA_{300}, and PDA_{500}, respectively) as confirmed by transmission electron microscopy (TEM), scanning electron microscopy (SEM), and multi-laser nanoparticle tracking analysis (M-NTA) (Figure 2c and Figure S2). The size was adjusted by varying the amount of dopamine feed (2–4 mg/ml) used for the reaction. The particle size confirmed by M-NTA was consistent with dynamic light scattering (DLS) data, showing that different-sized spherical PDA nanoparticles were uniform and monodispersed (PDI: 0.15 ± 0.02 (PDA_{70}), 0.08 ± 0.01 (PDA_{120}), 0.03 ± 0.01 (PDA_{300}), 0.1 ± 0.02 (PDA_{500})) (Figure 2d and Figure S3). The formation of PDA nanoparticles occurred under basic condition (pH 12), which induced self-oxidization and polymerization (Figure 2e). Fourier transform infrared spectra (FTIR) data confirmed peaks at 1,303, 1,510, and 1,602 cm^{-1} attributed to the C-N stretching of the indole ring, the C=N of the indole imine, and the C=C of the benzene ring, respectively (Figure 2f).[39]

The extinction coefficient of the synthetic melanin (*i.e.,* PDA_{70}) increased from 820 to 300 nm similar to that of real melanin (Figure 2g and Table S1).[40,41] PDA_{500} showed higher extinction than PDA_{120} at the same number (#*N*) of nanoparticle due to higher light absorption (μ_a, 97-fold), scattering (μ_s', 86-fold), and larger absorption cross-sectional area (18-fold). (Figure S4–5). These observations are consistent with Mie theory and the literature.[42–44] Accordingly, PA signal and spectra of PDA_{500} at the same #*N* was higher than that of PDA_{70} (450-fold), PDA_{120} (90-fold), and PDA_{300} (3-fold), respectively, because PA signal is a function of optical absorption (Figure 2h and Figure S6–7). In addition to the light absorption, PA signal generation also depends on specific heat capacity, laser fluence, and thermal expansion coefficient.[45] To further study the impact of particle size on PA signal generation, we hold constant extinction values of different-sized PDAs at 680 nm (Figure 2i). Although PDA_{120} had 12.8-fold higher concentration than PDA_{500} at the same extinction (Figure S8 and Movie S1–2), overall μ_s' of different-sized PDAs were similar at 680 nm likely due to the decreased light scattering from the size reduction (Figure S9 and table S2).[42,44] Importantly, PDA_{500} still showed higher PA signal and spectra than PDA_{70} (2.3-fold), PDA_{120} (1.9-fold), and PDA_{300} (1.5-fold), respectively at the same extinction of 0.3 at 680 nm (Figure 2i and Figure S7). This results indicate that PA signal generation

also depends on size-dependent thermal expansion coefficient, and the specific heat capacity (C_p) in which C_p increases with decreasing in particle size due to higher thermal vibration energy of surface atoms.[46] In addition, a single PDA_{500} nanoparticle has more surface area to transmit heat to the environment than a single PDA_{120} nanoparticle. In summary, PDA_{500} generated higher PA signal than PDA_{120} both at the same #N (90-fold) and at the same extinction (1.9-fold) due to the large optical absorption (Figure S4), absorption cross-sectional area (Figure S5), surface area, and heat capacity.[45,46]

Cluster-dependent PA performance.

Melanosomes are individually distributed or form clusters in the human skin.[31] To investigate the function of clusters of melanosomes, various metal ions (Na^+, Mg^{2+}, Fe^{2+}, Ca^{2+}) and other stimuli (NaOH, HCl, sugar, cysteine (Cys)) were applied to make PDA clusters. Metal ions induce PDA clustering because the catechol group in PDA can chelate metal ions, thus forming metal-phenolic networks (Figure S10).[37,47] The PA signal increased as PDA nanoparticles were clustered as assessed by DLS and inductively coupled plasma-mass-spectrometry (ICP-MS) (Figure 3a and Figure S11), and there was no background PA signal from Ca^{2+} only (Figure S12). The highest PA signal was observed in Ca^{2+} which caused significant PDA_{120} aggregation because of its strong binding affinity among the tested metal ions (Figure 3a and Figure S13).[48] Different Ca^{2+} concentrations (2–200 mM) were used to study the relationship between cluster size and PA signal. The results showed that PDA clusters induced by 200 mM of Ca^{2+} led to a 1.84-fold higher PA signal than PDA clusters induced by 20 mM of Ca^{2+}. There was no increase in PA signal at low Ca^{2+} concentrations (*e.g.,* 2–5 mM) because this concentration could not induce PDA clusters (Figure 3b). The formation of PDA clusters significantly decreased the extinction in the range of 400–550 nm while the extinction was increased from 552 to 900 nm likely due to the increased scattering by larger aggregates (Figure 3c and Figure S14).

We could disassemble PDA clusters *via* the strong chelating agent ethylenediaminetetraacetic acid (EDTA). After adding EDTA, PDA clusters were entirely disassembled due to the breakdown of metal coordination bonds (Figure S15). Collectively, the metal chelation was a dominant driving force for PDA clusters.[37] The PA signal of PDA clusters can be activated and deactivated by repeatedly adding EDTA and Ca^{2+} ions over four cycles (Figure 3d and Figure S16). We explained this increase in PA signal of PDA clusters through two reasons. First, the increased particle size by clustering could have a larger absorption cross-sectional area than small individuals.[31] The ~1 μm PDA clusters have 579-fold larger cross-sectional area than PDA_{120}. Second, PA signal is a function of thermoelastic expansion that occurs when the surrounding medium is locally heated. The aggregated nanoparticles could cause overlapping thermal fields that improve the rate of heat transfer and amplify PA signal.[28,49]

Human skin involves different-sized melanosomes, and thus we also studied the PA signal of PDA mixtures that contained both PDA_{300} and PDA_{120} at different ratios. The PDA mixture containing 66% of PDA_{300} and 33% of PDA_{120} had 1.8-fold higher PA signal than the PDA mixture containing 33% of PDA_{300} and 66% of PDA_{120} (Figure 3e). In addition, the PA signal of the PDA mixtures further increase by Ca^{2+}-induced PDA clustering. Notably, PDA

clusters formed by PDA_{120} exhibited significantly higher (10.5-fold) PA signal than PDA_{120} while the PDA clusters formed by PDA_{300} only increased 1.13-fold, thus indicating that this aggregation-derived PA signal is affected by particle size. To understand the relationship between particle size and aggregation, we used M-NTA to monitor aggregation of PDA mixtures (Figure 3f and Figure S17). The results showed that PDA_{120} were more prone to aggregate than PDA_{300} because small nanoparticles have a higher surface area-to-volume ratio, which implies a higher surface energy than the large particles (Figure S18).[50] This explains why PDA_{120} dramatically increased their size (from 120 nm to >1 μm), thus significantly increasing PA signal. In summary, our PA experiments revealed that the PA signal of PDA can be improved by increasing (i) size (>90-fold: PDA_{500} *versus* PDA_{120}), (ii) clustering (2–10.5-fold:10 mM *versus* 200 mM Ca^{2+}), and (iii) concentration (1.3–8-fold: 1 μg/ml *versus* 8 μg/ml of PDA mixtures).

To use these materials in a phantom, we used a GelMA-based scaffold which can provide three dimensional supports with characteristics of the native extracellular matrix (Figure S19). The average thicknesses of dermis and epidermis in human skin are 2.5 mm and 0.2 mm, respectively,[51] and thus GelMA hydrogel with a thickness of 2.5 mm was first printed to provide the baseline of the epidermis. A PDA-included hydrogel with a thickness of 0.2 mm was then built on the top to mimic human skin phototypes (Movie S3). The dimension (20 mm × 20 mm × 2.7 mm) of the printed sample was precisely adjustable using 3D-bioprinting. Finally, UV light (365 nm) was used to initiate radical polymerization and form covalently crosslinked hydrogels (Figure 3g).

To study the function of PDA clusters when bio-printed, we next prepared three different bio-inks containing clustered PDAs by using 0, 20, and 200 mM Ca^{2+}. Each bio-ink had the same total number of PDA_{120} and PDA_{300}. 3D-bioprinted PDA with 200 mM of Ca^{2+} showed 3-fold higher PA signal than PDA with 20 mM of Ca^{2+}. There was significantly (>10-fold) higher PA signal than PDA with 0 mM of Ca^{2+} similar to the solution phase data in Figure 3e. We also found that the number of PA peaks exponentially increased corresponding to the number of induced PDA clusters: The printed samples with 0-, 20-, and 200-mM of Ca^{2+} showed 2, 11, and 85 of PA peak clusters, respectively (Figure 3h and Figure S20). In contrast, all three printed samples had the same international commission in illumination (CIE) coordinates of Fitz. 6 (*i.e.,* skin phototype), thus indicating that skin phototype is more correlated with the number of PDA *nanoparticles* than the PDA clusters (Figure 3i).

PA characterization of real and mimicked human skin.

Melanosomes have been intensively characterized and studied in dermatology.[9,31,52] A recent study measured variable melanosome contents in the different human skin phototypes. It showed that Fitz. 5 human skin contained more and larger melanin than Fitz. 2 human skin; melanin clusters were more often found in Fitz. 2 skin (Figure S21).[31] To mimic the variable contents of melanosomes, we used PDA mixtures composed of PDA clusters, PDA_{120}, and PDA_{300}. Both real and mimicked human skins had the same thickness of epidermis (about 0.2 mm) and contained melanin with the same color scale (Figure 4a and Figure S22). Different ratios of individual and clustered PDAs were mixed to understand

the relationship between PDA contents *versus* variable skin phototypes. The results showed that skin phototypes are predominantly dependent on the particle concentration (M_f) rather than particle size or PDA clusters (Figure 4b and Figure S23). As PDA concentration increases (from 1- to 8-fold), PA signal linearly increased from 1.3- to 8-fold, and the color of skin phototype changed from Fitz. 1 to Fitz. 6. In addition, PDA_{120}, PDA_{300}, and PDA clusters were arbitrarily distributed and maintained their spherical shapes in the epidermis of printed skin phantom as confirmed by SEM (Figure 4c).

PA signal of our mimicked skins was matched to that of real human skins: Fitz. 5 skin had 3.5-fold higher PA signal than Fitz. 2 skin in both real and mimicked samples (Figure 4d). Furthermore, the PA images of real and mimicked skins visualized melanin distribution, indicating that both real and synthetic melanin were randomly distributed; strong PA signal peaks were found where melanosomes were crowded and/or clustered (Figure 4e–f and Figure S24). Real and mimicked skins showed a comparable PA spectrum from 680 nm to 970 nm (Figure 4g). The mimicked skin had stable PA signal for 5 min implying stable PDA mixtures under the 680-nm laser illumination (Figure 4h). Ultrasound (US) images revealed 4 mm thickness of human skin composed of the epidermis, dermis, and hypodermis. A strong PA signal was exclusively observed in the basal layer of epidermis where most melanosomes were located (Figure 4i). Likewise, mimicked skins had comparable skin thickness and strong PA signal generated from the epidermis. There was no decrease in sample thickness and PA signal of Fitz. 2 and 5 skin phantoms for 7 days (Figure S25). Finally, we inverted the Fitz. 2 and Fitz. 5 human skin samples to investigate tissue scattering in the underlying fat tissue layers of the dermis. No PA signal was observed in the epidermis of either human skin sample due to large light scattering in the dermis. The fat tissue layers in the dermis have low absorption at 680 nm to generate PA signal (Figure 4j and Figure S26).

Impact of skin phototype on biomedical optic modalities.

3D-bioprinted phantoms with skin phototypes from Fitz. 1 to 6 were successfully developed by adjusting the PDA contents used for bio-inks: Fitz. 1, Fitz. 3, and Fitz. 5 contained a M_f of 3%, 12%, and 20%, respectively (Figure S27). The phantom without skin prototype was also fabricated as a negative control (referred to as Fitz. 0). Both the CIE color space and a colorimeter were used to quantify our phantoms with different skin phototypes (Figure S28 and Table S3). Titanium oxide (TiO_2) was also used to mimic tissue scattering in the dermis.[53] We then measured the energy attenuation from 680, 800, and 1064 nm laser beams caused by the mimicked skin phototypes (Figure 5a). The results showed that darker skin attenuated more laser energy (mJ) than lighter skin: Fitz. 1, 3, and 5 skin phantoms decreased 1, 3, and 6 mJ energy at 680 nm which is relevant to the absorption peak of deoxyhemoglobin (660 nm).[23] Moreover, the 680-nm laser attenuated 1.3- and 1.98-fold more energy than 800 nm and 1064 nm lasers, respectively, because of higher light absorption and scattering of synthetic melanin. To further evaluate this, the absorption coefficient (μ_a) and the reduced scattering coefficient (μ_s') of skin-tone phantoms (Fitz. 1, 3, and 5) were characterized using the inverse adding double (IAD) manual based on reflectance and transmittance measurements of samples in an integrating sphere spectrophotometer (the detailed calculation is described in supplementary information).[54,55]

Both the μ_a and μ_s' of mimicked skin phototypes exponentially increased from 400−600 nm and linearly in the 600–900 nm region: The μ_a of Fitz. 5 at 680 nm was 1.37-fold higher than that at 800 nm (Figure 5b). More importantly, μ_a (1.03 mm^{-1}) and μ_s' (4.34 mm^{-1}) values of our mimicked skins were comparable to that of real human skins (μ_a (0.72 ± 0.29 mm^{-1}) and μ_s' (4.89 ± 1.15 mm^{-1}) at 694 nm) (see Table S4).[12,56] The μ_a and μ_s' of 3D-bioprinted phantoms were tunable by controlling the particle ratio between PDA_{300} and PDA_{120} in the epidermis. For example, the μ_a of the Fitz. 1 skin phantom with 100% of PDA_{300} showed a 1.1-fold higher than that of Fitz. 1 skin phantom with 100% PDA_{120}.

We next used these mimicked skin-tone phantoms to study the impact of skin phototypes on biomedical optics technology including PA imaging, fluorescence imaging, and photothermal therapy. For PA imaging, methylene blue (MB) and indocyanine green (ICG) dyes were chosen as contrast agents to demonstrate the utility of the phantom at 680 nm and 800 nm, respectively. Here, MB and ICG dyes (100 μM to 25 mM) were linearly aligned in the tubes and imaged under the Fitz. 1, 3, and 5 skin phantoms (Figure 5c and Figure S29). The PA signal and spectra of the ICG dye was less compromised by skin phototypes *versus* MB dye (Figure S30–31). Specifically, MB dye showed 14%, 55%, and 65% PA signal attenuation with Fitz. 1, 3, and 5 skin. ICG showed a 10%, 37%, and 55% decrease in PA signal at the same dye concentration (Figure 5d). Samples in the yellow dotted area in Figure 5c were intentionally uncovered to show that there was no decrease in laser power and/or photobleaching of the dye during the measurement. We further studied the imaging depth of MB and ICG dye with the phantoms. The 5-mm-thick GelMA phantom including TiO_2 (0.5 mg/ml) was 3D-printed, and each sample was injected at heights 1 mm apart (Figure 5e and Figure S32). The Fitz. 5 skin phantom has PA signal of MB dye that was attenuated by 44%, 97%, and 100% at depths of 1, 2, and 3 mm, respectively. The PA signal of the ICG dye was decreased by 43%, 63%, and 85% of PA signals at the same depths (Figure 5f). These results indicated that ICG dye had higher imaging depth due to its longer absorption wavelength (800 nm). In this NIR region, melanin has lower light absorption and scattering. We further designed a blood vessel scaffold to measure the PA signal of real human blood under different skin phototypes to investigate the impact of imaging deoxyhemoglobin (Figure S33). PA images showed that 33%, 52%, and 70% of PA signals decreased under the Fitz. 1, 3, and 5 skin phantoms. There was a yellow dotted area that remained uncovered. This showed no decrease in laser power or sample degradation (Figure 5g).

Fluorescence could also be affected by melanin. Thus, cyanine5.5 (Cy5.5) and ICG dyes at the same dye concentration (100 μM) were used to evaluate the impact of skin phototypes on their corresponding excitation (*i.e.,* 680 and 800 nm, respectively). Not surprisingly, Cy5.5 signal decreased by 32% and 69% under the Fitz. 3 and 5 phantoms, respectively; the ICG dye only decreased by 6% and 53%, thus confirming the wavelength-dependent fluorescence attenuation (Figure 5h). Photothermal therapy also often uses near-infrared (NIR) light. Here, gold nanorods (GNRs) with two different aspect ratios (*e.g.,* 3.3 and 7.3) were synthesized and had a longitudinal absorption peak at 800 nm and 1062 nm, respectively (Figure S34). Two different NIR lasers (*i.e.,* 808 and 1064 nm) were used to irradiate GNRs at an O.D. (= 1) underneath different skin phantoms. A thermal camera was used to record the temperature (Figure 5i). The results revealed that the temperature increase facilitated by the GNRs decreased as a function of phototype: Fitz. 1 (8%), Fitz. 3 (14%),

and Fitz. 5 (17%) *versus* Fitz. 0 when irradiated by the 808 nm laser. GNRs irradiated by 1064 nm exhibited relatively minor decreases in temperature: Fitz. 1 (4%), Fitz. 3 (7%), and Fitz. 5 (8%). The 1064 nm (NIR-II) laser was significantly less influenced by skin phototypes.

Conclusions

Phantom-based testing is a powerful approach to evaluate the performance of various optical devices and judge quality of medical imaging without risks to human. Skin-mimicking acellular phantoms have been developed for biomedical optics.[23,57–60] One phantom used gelatin and synthetic melanin to make 0.1 mm-thick epidermal layer and characterized tunable mechanical, optical and acoustic properties.[57] However, this hydrogel-based phantom is limited to control the thickness of each layer and needs vacuum sealed container for storage. In other study, polydimethylsiloxane (PDMS) silicone and ground coffee were used to make tissue-mimicking phantom.[60] Although PDMS-based phantom provides high stability and simplicity, ground coffee is limited to mimic optical absorption of real human skin. To improve this, one recent study used synthetic melanin with PDMS and showed high stability with comparable absorption values to real human skin.[23] However, synthetic melanin used in the previous studies[23,57,59,60] is a form of solid powder (*i.e.,* small molecule) which lacks of bio-relevant size and shape to real melanosomes. All the phantoms used different powder concentrations to achieve different skin pigmentation levels which could lose scattering component of real melanosomes. Furthermore, they have not validated the impact of skin tones on biomedical imaging equipment.

Here we developed skin-mimicking phantoms with synthetic melanin *(i.e.,* PDA) as a tool to quantify the impact of skin phototypes on multiple biomedical optics (*e.g.,* PA, photothermal, and fluorescence imaging). To mimic optical properties of melanin, we investigated the light absorption of spherical PDAs in different sizes, mixtures, and clustering phases. Our skin phantoms are enabled by 3D bioprinting which provides precise deposition of biomaterials, high controllability, good reproducibility, and low cost compared to mold-based phantom fabrications.[61] Human skin consists of multiple thin layers with different thicknesses (0.1–5 mm) and materials, indicating that bioprinting could provide a better platform to mimic the human skin.[61–63] 3D bioprinting also offers customized phantom designs for testing various target of interests (*e.g.,* imaging depth and blood vessel) for medical imaging devices. GelMA-based scaffolds could serve as extracellular matrix for cell growth, providing more opportunities for deciphering the role of melanin in cell regeneration against UV-light as a future study.[62,64] Our skin phantoms will provide quantitative data of skin tone impact for other biomedical optics (*e.g.,* pulse oximeter, wearables) to deliver more accurate and objective assessments of the device performance. Finally, our methods possibly motivate more phantom studies and will improve device instrumentation and algorithms to correct for race-based bias in biomedical optics.

Experimental Section

Synthesis of GelMA hydrogel

Briefly, gelatin from a porcine skin was fully dissolved in PBS (10% w/v) at 55 C°, and then methacrylic anhydride (MA) was added dropwise (0.5 ml/min) until the target volume reached.[32] For the methacrylation reaction, the mixture was vigorously stirred at 1000 rpm for 2 h. The solution was then centrifuged at 1000 g for 2 min to remove excess MA. Supernatants were diluted five times with additional PBS to stop the reaction followed by dialysis against distilled water (12–14 kDa cut-off, refreshed water five times) for 5 days at 40 C°. Unreacted MA and salts were further removed during the dialysis. The GelMA hydrogel was placed at –80 C° overnight and lyophilized for 5 days, thus forming a porous white foam. The product was stored at –80 C° for future use (Figure S35).

Synthesis of synthetic melanin

Briefly, 5 ml of distilled water and 2 ml of ethanol were mixed under vigorous stirring at room temperature followed by addition of 500 μL of fresh dopamine solution (40 mg/mL in distilled water).[35] Then, 100 μL of ammonium hydroxide solution was added to trigger the polymerization. The color immediately changed from yellow to dark brown within 20 minutes. The solution was stirred at 900 rpm overnight. The size of the polydopamine could be readily controlled by adjusting the amount of dopamine. For example, 500, 600, 700, and 800 μL of dopamine solution forms polydopamine with sizes of 70, 120, 300, and 500, respectively. The samples were purified with centrifugation at 14,000 *g* (for PDA_{70}), 7,000 *g* (for PDA_{120}), 2,000 *g* (for PDA_{300}), and 1,000 *g* (for PDA_{500}) for 10 min. The pellet was redispersed in water for future use.

Bio-ink preparation and bio-printing procedure

Briefly, freeze-dried GelMA macromers were dissolved in PBS (10% w/v) at 50 C° for 20 minfollowed by adding alginic acid (4% w/v) and photo-initiator (0.5% w/v).[65] During bio-ink preparation, the sample was covered by aluminum foil (to prevent photo-crosslink from the light) and gently mixed for 1 h. Synthetic melanin was added in GelMA macromer before adding the photo-initiator. Different skin phototypes were readily tunable by adjusting different amounts of synthetic melanin in GelMA macromer. For example, 4, 8, 12, 16, 20, and 30 μL of PDA mixtures (0.01 mg/ml) that contain 20% of PDA clusters, 30% of PDA_{120}, and 50% of PDA_{300} were mixed with 1 mL of GelMA macromer to prepare bio-inks for different skin phototypes from Fitz. 1 (4 μL) to Fitz. 6 (30 μL). In addition, the 10 – 100 μL of PDA mixtures were deposited on the interface between the epidermis and the dermis to mimic basal layers (the innermost layer of the epidermis) where most of melanin resides. The prepared bio-inks were then stored at 4 C° and warmed at 37 C° for 30 min before use. The 3D-bioprinting procedure was performed using an BioX 3D bioprinter (CELLINK+). Printing parameters (*e.g.,* temperature, pressure, speed) influence the printing quality and distribution of synthetic melanin. First, printing temperature was controlled at room temperature (25 C°) where bio-ink maintains its gel-like viscosity. Second, printing pressure is correlated with diameter of needle and printing speed. Notably, different-sized needle (*e.g.,* diameter, length) requires different printing pressure and speed. In this study, gauge size and length of needle were 20 G and length 0.25’ inch. Printing pressure was

controlled at 20–70 kPa pressure. Otherwise, high pressure (>150 kPa) extruded bio-ink irregularly. Lastly, printing speed was controlled at 1.5–2.5 mm/s. After bioprinting, 365 nm of UV light with an intensity of 25 mW/cm^2 was used to trigger photo-crosslinking for 5 min. Specifically, good bioprinting quality could be achieved by careful selections of the needle (*e.g.,* gauge (20G)), printing speed (2 mm/s), pressure (25 kPa), temperature (25 C°) as well as the rheology of the bio-ink. The printed skin phantoms were then stored in a petri dish sealed with parafilm covered by aluminum foil for future use.

Photoacoustic imaging of human skin specimens

All work with human subjects was done in accordance with institutional review board (IRB) guidelines and approval (project #191998X). Two human skin tissues (15 cm × 15 cm, white and dark) were donated from UCSD and UCI Health Centers. Whole human blood was collected from a healthy donor following guidelines. Informed consent of all participants was obtained prior to the experiment. Human skin samples were stored in –80 C°. Prior to the experiments, the skin was thawed at the room temperature and razor blades were used to cut the skin specimens with the size of 2 cm × 2 cm. The specimens were immersed in the formalin fixation buffer overnight. PA imaging was acquired using a Vevo 2100 LAZR (Visual Sonic, USA), with a 21 MHz transducer (LZ-250). Laser intensity was optimized and calibrated. *ex vivo* human skin specimens were cleaned three times with deionized water before and after the PA measurements.

Supplementary Material

Refer to Web version on PubMed Central for supplementary material.

Acknowledgement

The authors wish to thank the individuals who donated their bodies and tissues for the advancement of education and research. This work was supported by National Science Foundation (#1937674 and #2149602) and National Institutes of Health (T32AR064194, and R03DE031009). This work was performed in part at San Diego Nanotechnology Infrastructure (SDNI) of University of California San Diego supported by (NSF ECCS-1542148), and by the Cellular and Molecular Medicine Electron Microscopy core facility (NIH S10 OD 023527). This work was also supported by National Science Foundation (DMR-2011924) through the UC San Diego Materials Research Science and Engineering Center (UCSD MRSEC). The authors also thanks Sunwoo Kwak for technical support for artwork, and Dr. Lingyan Shi, and Dr. Ali Hariri for helpful discussions.

Data availability

The main data supporting the findings in this study are accessible within the paper and its supplementary information. Source data for the figures are available for research purposes from the corresponding author upon request.

Abbreviations

PA	photoacoustic
US	ultrasound
UV	ultraviolet

Fitz	Fitzpatrick
M_f	melanosome volume fraction
GelMA	gelatin methacrylate
PDA	polydopamine
PDA_{70}	polydopamine with the diameter of 70 nm
PDA_{120}	polydopamine with the diameter of 120 nm
PDA_{300}	polydopamine with the diameter of 300 nm
PDA_{500}	polydopamine with the diameter of 500 nm
MB	methylene blue
ICG	indocyanine green
Cy5.5	cyanine5.5
TEM	transmission electron microscopy
SEM	scanning electron microscopy
EDX	energy dispersive X-ray spectroscopy
M-NTA	multi-laser nanoparticle tracking analysis
DLS	dynamic light scattering
PDI	polydispersity index
FTIR	Fourier transform infrared spectra
C_p	heat capacity
UV-vis	ultraviolet-visible
MS-ICP	inductively coupled plasma-mass-spectrometry
Cys	cysteine
EDTA	ethylenediaminetetraacetic acid
CIE	International commission in illumination
TiO_2	titanium oxide
μ_a	absorption coefficient
μ_s'	reduced scattering coefficient
IAD	inverse adding double
OCT	optical coherence tomography

MA	methacrylic anhydride
NIR-II	second-near infrared
PDMS	polydimethylsiloxane

REFERENCES

1. Dyring-Andersen B et al. Spatially and cell-type resolved quantitative proteomic atlas of healthy human skin. Nat. Commun. 11, 1–14 (2020). [PubMed: 31911652]
2. Natarajan VT, Ganju P, Ramkumar A, Grover R & Gokhale RS Multifaceted pathways protect human skin from UV radiation. Nat. Chem. Biol. 10, 542–551 (2014). [PubMed: 24937072]
3. Lechler T & Fuchs E Asymmetric cell divisions promote stratification and differentiation of mammalian skin. Nature 437, 275–280 (2005). [PubMed: 16094321]
4. Bowden GT Prevention of non-melanoma skin cancer by targeting ultraviolet-B-light signalling. Nat. Rev. Cancer 4, 23–35 (2004). [PubMed: 14681688]
5. Bald T et al. Ultraviolet-radiation-induced inflammation promotes angiotropism and metastasis in melanoma. Nature 507, 109–113 (2014). [PubMed: 24572365]
6. Epstein JH Photocarcinogenesis, skin cancer, and aging. J. Am. Acad. Dermatol. 9, 487–502 (1983). [PubMed: 6355213]
7. Eller MS, Yaar M & Gilchrest BA DNA damage and melanogenesis. Nature 372, 413–414 (1994). [PubMed: 7984233]
8. Wicks NL, Chan JW, Najera JA, Ciriello JM & Oancea E UVA phototransduction drives early melanin synthesis in human melanocytes. Curr. Biol. 21, 1906–1911 (2011). [PubMed: 22055294]
9. Thong HY, Jee SH, Sun CC & Boissy R The patterns of melanosome distribution in keratinocytes of human skin as one determining factor of skin colour. Bri. J. Dermatol. 149, 498–505 (2003).
10. Jacques SL Origins of tissue optical properties in the UVA, visible, and NIR regions. OSA TOPS on advances in optical imaging and photon migration 2, 364–369 (1996).
11. Ou-Yang H, Stamatas G & Kollias N Spectral responses of melanin to ultraviolet A irradiation. J. Invest. Dermatol. 122, 492–496 (2004). [PubMed: 15009735]
12. Jacques SL Optical properties of biological tissues: a review. Phys. Med. Biol. 58, R37 (2013). [PubMed: 23666068]
13. Sjoding MW, Dickson RP, Iwashyna TJ, Gay SE & Valley TS Racial bias in pulse oximetry measurement. N. Engl. J. Med. 383, 2477–2478 (2020). [PubMed: 33326721]
14. Gottlieb ER, Ziegler J, Morley K, Rush B & Celi LA Assessment of racial and ethnic differences in oxygen supplementation among patients in the intensive care unit. JAMA Intern. Med. 182, 849–858 (2022). [PubMed: 35816344]
15. Bickler PE, Feiner JR & Rollins MD Factors affecting the performance of 5 cerebral oximeters during hypoxia in healthy volunteers. Anesth. Analg. 117, 813–823 (2013). [PubMed: 24023027]
16. O'Rese JK et al. Effect of race, age, and axial length on optic nerve head parameters and retinal nerve fiber layer thickness measured by Cirrus HD-OCT. Arch. Ophthalmol. 130, 312–318 (2012). [PubMed: 22411660]
17. Bent B, Goldstein BA, Kibbe WA & Dunn JP Investigating sources of inaccuracy in wearable optical heart rate sensors. NPJ Digit. Med. 3, 1–9 (2020). [PubMed: 31934645]
18. Ray I, Liaqat D, Gabel M & de Lara E Skin tone, confidence, and data quality of heart rate sensing in WearOS smartwatches. Proc. IEEE, 213–219 (2021).
19. Colvonen PJ, DeYoung PN, Bosompra N-OA & Owens RL Vol. 43 zsaa159 (Oxford University Press US, 2020).
20. Li X et al. Optoacoustic mesoscopy analysis and quantitative estimation of specific imaging metrics in Fitzpatrick skin phototypes II to V. J. Biophotonics 12, e201800442 (2019). [PubMed: 31012286]
21. Rennie MY et al. Understanding real-time fluorescence signals from bacteria and wound tissues observed with the MolecuLight i: XTM. Diagnostics 9, 22 (2019). [PubMed: 30813551]

22. Joensen J et al. The thermal effects of therapeutic lasers with 810 and 904 nm wavelengths on human skin. Photomed. Laser Surg. 29, 145–153 (2011). [PubMed: 21219241]
23. Afshari A et al. Evaluation of the robustness of cerebral oximetry to variations in skin pigmentation using a tissue-simulating phantom. Biomed. Opt. Express 13, 2909–2928 (2022). [PubMed: 35774336]
24. Saager RB, Quach A, Rowland RA, Baldado ML & Durkin AJ Low-cost tissue simulating phantoms with adjustable wavelength-dependent scattering properties in the visible and infrared ranges. J. Biomed. Opt. 21, 067001 (2016). [PubMed: 27292135]
25. Roberts WE Skin type classification systems old and new. Dermatol. Clin. 27, 529–533 (2009). [PubMed: 19850202]
26. Mantri Y & Jokerst JV Impact of skin tone on photoacoustic oximetry and tools to minimize bias. Biomed. Opt. Express 13, 875–887 (2022). [PubMed: 35284157]
27. Chen R et al. Photoacoustic molecular imaging-escorted adipose photodynamic–browning synergy for fighting obesity with virus-like complexes. Nat. Nanotechnol. 16, 455–465 (2021). [PubMed: 33526836]
28. Yim W et al. Enhanced photoacoustic detection of heparin in whole blood via melanin nanocapsules carrying molecular agents. ACS Nano (2021).
29. Wu Z et al. In vivo dual-scale photoacoustic surveillance and assessment of burn healing. Biomed. Opt. Express 10, 3425–3433 (2019). [PubMed: 31467787]
30. Yu Q et al. Label-free visualization of early cancer hepatic micrometastasis and intraoperative image-guided surgery by photoacoustic imaging. J. Nucl. Med. 61, 1079–1085 (2020). [PubMed: 31806769]
31. Hurbain I et al. Melanosome distribution in keratinocytes in different skin types: melanosome clusters are not degradative organelles. J. Invest. Dermatol. 138, 647–656 (2018). [PubMed: 29054596]
32. Nichol JW et al. Cell-laden microengineered gelatin methacrylate hydrogels. Biomaterials 31, 5536–5544 (2010). [PubMed: 20417964]
33. Riley PA Melanin. Int. J. Biochem. Cell Biol. 29, 1235–1239 (1997). [PubMed: 9451820]
34. Pralea I-E et al. From extraction to advanced analytical methods: The challenges of melanin analysis. Int. J. Mol. Sci. 20, 3943 (2019). [PubMed: 31412656]
35. Lee H, Dellatore SM, Miller WM & Messersmith PB Mussel-inspired surface chemistry for multifunctional coatings. Science 318, 426–430 (2007). [PubMed: 17947576]
36. Battistella C et al. Mimicking natural human hair pigmentation with synthetic melanin. ACS Cent. Sci. 6, 1179–1188 (2020). [PubMed: 32724852]
37. Wu D et al. Phenolic-enabled nanotechnology: versatile particle engineering for biomedicine. Chem. Soc. Rev. 50, 4432–4483 (2021). [PubMed: 33595004]
38. Yim W et al. Gold nanorod–melanin hybrids for enhanced and prolonged photoacoustic imaging in the near-infrared-II window. ACS Appl. Mater. Interfaces 13, 14974–14984 (2021). [PubMed: 33761255]
39. Patel K et al. Polydopamine films change their physicochemical and antimicrobial properties with a change in reaction conditions. Phys. Chem. Chem. Phys. 20, 5744–5755 (2018). [PubMed: 29411802]
40. Crippa P, Cristofoletti V & Romeo N A band model for melanin deduced from optical absorption and photoconductivity experiments. Biochim. Biophys. Acta -Gen. Su. 538, 164–170 (1978).
41. Sarna T & Sealy R Photoinduced oxygen consumption in melanin systems. Action spectra and quantum yields for eumelanin and synthetic melanin. Photochem. Photobiol. 39, 69–74 (1984). [PubMed: 6422483]
42. Fu Q & Sun W Mie theory for light scattering by a spherical particle in an absorbing medium. Appl. Opt. 40, 1354–1361 (2001). [PubMed: 18357121]
43. Shang J & Gao X Nanoparticle counting: towards accurate determination of the molar concentration. Chem. Soc. Rev. 43, 7267–7278 (2014). [PubMed: 25099190]

44. Pu Y, Chen J, Wang W & Alfano RR Basic optical scattering parameter of the brain and prostate tissues in the spectral range of 400–2400 nm. Neurophotonics and Biomedical Spectroscopy, 229–252 (2019).
45. Mantri Y & Jokerst JV Engineering plasmonic nanoparticles for enhanced photoacoustic imaging. ACS Nano 14, 9408–9422 (2020). [PubMed: 32806027]
46. Wang B-X, Zhou L-P & Peng X-F Surface and size effects on the specific heat capacity of nanoparticles. Int. J. Thermophys. 27, 139–151 (2006).
47. Ejima H et al. One-step assembly of coordination complexes for versatile film and particle engineering. Science 341, 154–157 (2013). [PubMed: 23846899]
48. Fan Z, Sun L, Huang Y, Wang Y & Zhang M Bioinspired fluorescent dipeptide nanoparticles for targeted cancer cell imaging and real-time monitoring of drug release. Nat. Nanotech. 11, 388–394 (2016).
49. Bayer CL, Nam SY, Chen Y-S & Emelianov SY Photoacoustic signal amplification through plasmonic nanoparticle aggregation. J. Biomed. Opt. 18, 016001 (2013). [PubMed: 23288414]
50. Zhang W Nanoparticle aggregation: principles and modeling. Nanomater., 19–43 (2014).
51. Branchet M, Boisnic S, Frances C & Robert A Skin thickness changes in normal aging skin. Gerontology 36, 28–35 (1990). [PubMed: 2384222]
52. Boissy RE Melanosome transfer to and translocation in the keratinocyte. Exp. Dermatol, 12, 5–12 (2003).
53. Hariri A et al. Polyacrylamide hydrogel phantoms for performance evaluation of multispectral photoacoustic imaging systems. Photoacoustics 22, 100245 (2021). [PubMed: 33747787]
54. Prahl SA, van Gemert MJ & Welch AJ Determining the optical properties of turbid media by using the adding–doubling method. Appl. Opt. 32, 559–568 (1993). [PubMed: 20802725]
55. Prahl SA in Optical-thermal response of laser-irradiated tissue 101–129 (Springer, 1995).
56. Shimojo Y, Nishimura T, Hazama H, Ozawa T & Awazu K Measurement of absorption and reduced scattering coefficients in Asian human epidermis, dermis, and subcutaneous fat tissues in the 400-to 1100-nm wavelength range for optical penetration depth and energy deposition analysis. J. Biomed. Opt. 25, 045002 (2020). [PubMed: 32356424]
57. Chen AI et al. Multilayered tissue mimicking skin and vessel phantoms with tunable mechanical, optical, and acoustic properties. Med. Phys. 43, 3117–3131 (2016). [PubMed: 27277058]
58. Saager RB, Cuccia DJ & Durkin AJ Determination of optical properties of turbid media spanning visible and near-infrared regimes via spatially modulated quantitative spectroscopy. J. Biomed. Opt. 15, 017012 (2010). [PubMed: 20210486]
59. Soyemi OO, Landry MR, Yang Y, Idwasi PO & Soller BR Skin color correction for tissue spectroscopy: demonstration of a novel approach with tissue-mimicking phantoms. Appl. Spectrosc. 59, 237–244 (2005). [PubMed: 15720765]
60. Saager RB et al. Multilayer silicone phantoms for the evaluation of quantitative optical techniques in skin imaging. Proc. SPIE 7567–06, 1–8 (2010).
61. Kang H-W et al. A 3D bioprinting system to produce human-scale tissue constructs with structural integrity. Nat. Biotechnol. 34, 312–319 (2016). [PubMed: 26878319]
62. Huyan Y, Lian Q, Zhao T, Li D & He J Pilot study of the biological properties and vascularization of 3D printed bilayer skin grafts. Int. J. Bioprinting. 6 (2020).
63. Ng WL, Qi JTZ, Yeong WY & Naing MW Proof-of-concept: 3D bioprinting of pigmented human skin constructs. Biofabrication 10, 025005 (2018). [PubMed: 29360631]
64. Yang JC et al. Electronic skin: recent progress and future prospects for skin-attachable devices for health monitoring, robotics, and prosthetics. Adv. Mater. 31, 1904765 (2019).
65. Barros NR et al. Biofabrication of endothelial cell, dermal fibroblast, and multilayered keratinocyte layers for skin tissue engineering. Biofabrication 13, 035030 (2021).

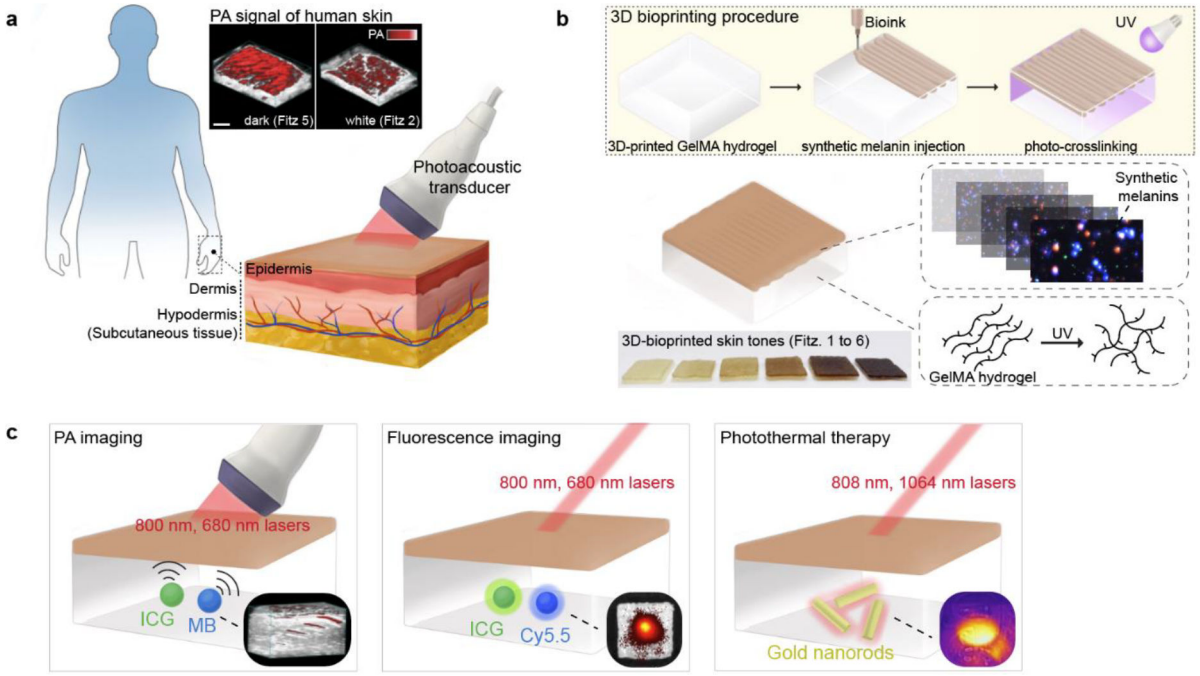

Figure 1. Mimicking human skin phototype for biomedical optics.

a, PA transducer imaged melanosomes in human skins of Fitz. 5 and Fitz. 2. The scale bar represents 4 mm. **b**, The 3D bioprinting procedure to mimic human skin phototypes using synthetic melanin and GelMA hydrogel. Red and blue dots in the insert image are real PDA nanoparticles measured by M-NTA. **c**, Evaluation of skin tone impact on multiple biomedical optics (*e.g.,* PA imaging, fluorescence imaging, and photothermal therapy). MB, ICG, Cy5.5, and gold nanorods were used to investigate the impact in different wavelengths (680–1064 nm). Insert images describe PA signal, fluorescence, and temperature of the probes under the skin-tone phantoms during the examination.

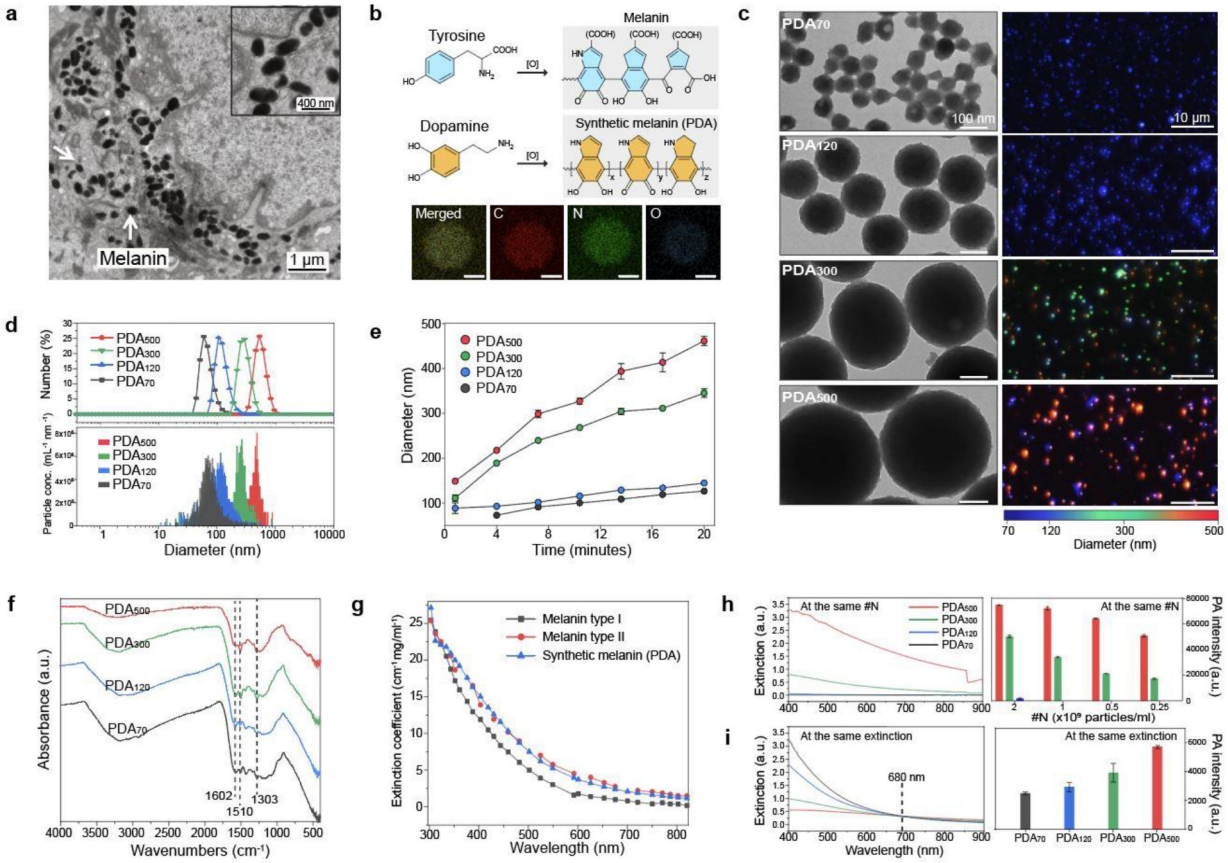

Figure 2. Material characterization of synthetic melanin.

a, TEM image of melanin in human skin. **b,** Chemical structure of melanin and synthetic melanin (PDA). EDX mapping showed that PDA consists of C, N, and O, *i.e.,* components of melanin in human skin. The scale bars represent 50 nm. **c,** TEM (left column) and M-NTA (right column) images of PDAs with different sizes from 70 to 500 nm. Blue (70–150 nm), green (300 nm), and red (>400 nm) dots represent actual PDAs scattered in the water during M-NTA measurements. **d,** Hydrodynamic diameter confirmed by DLS (top) and NTA (bottom). **e,** Oxidization process of dopamine, showing time-dependent PDA growth. **f,** FTIR data of PDA nanoparticles. The peaks in PDAs at 1303, 1510, and 1602 cm^{-1} indicate that PDAs consist of the indole structure. **g,** Extinction coefficients of real and synthetic melanin. Melanin type I and II indicate eumelanin and pheomelanin, respectively. **h,** Extinction spectra and the corresponding PA signals of different-sized PDAs at the same #*N* from 0.25 to 2 × 10^9 particles/ml. The red, green, and blue bars represent PDA_{500}, PDA_{300}, and PDA_{120}, respectively. **i,** Extinction spectra and the corresponding PA signals of different-sized PDAs at the same extinction of 0.3 at 680 nm. The error bars represent the standard deviation of six regions of interest. The experiment in h and i was repeated independently three times with similar results. Panel a and g reproduced with permission from Elsevier.[31,40,41]

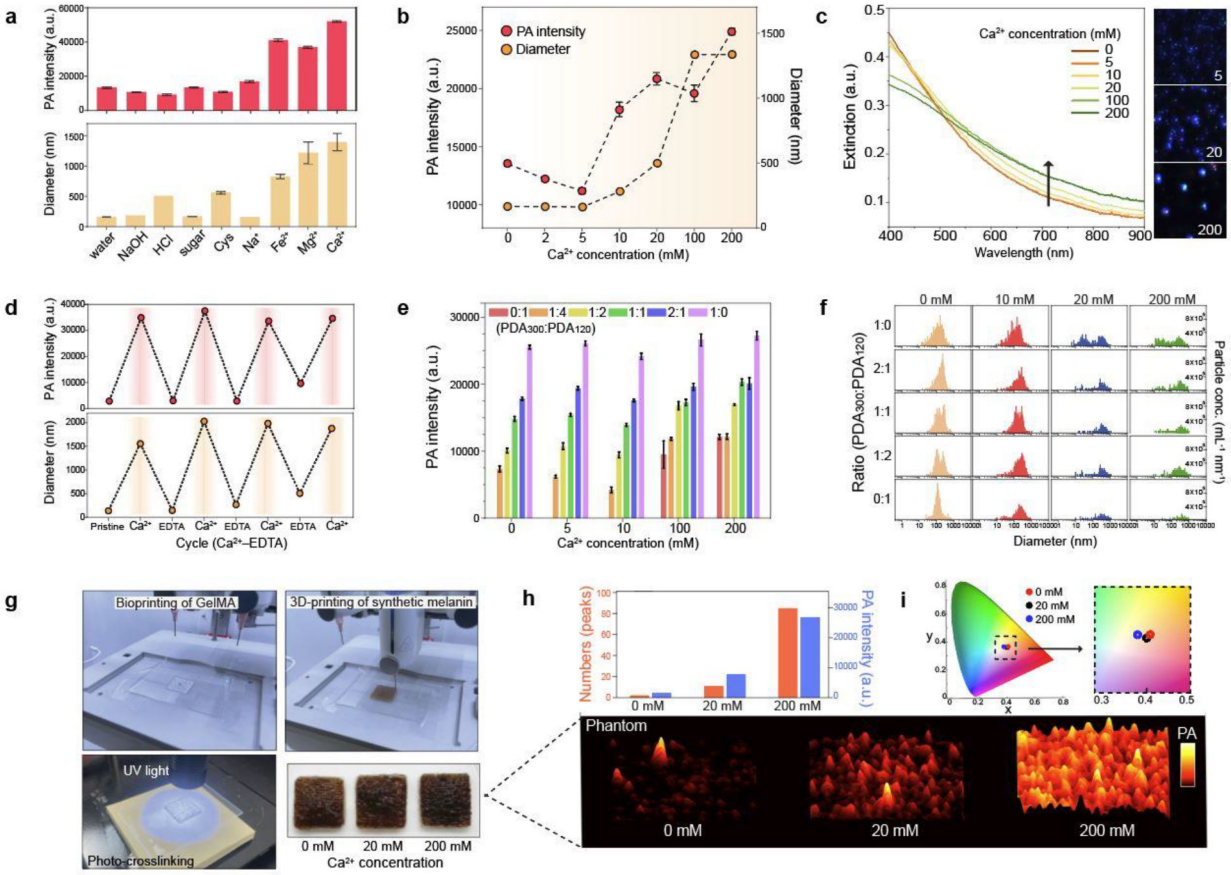

Figure 3. Clusters of synthetic melanin.

a, PA signal of PDA clusters. Different metal ions and other sample matrices were used to induce PDA clusters. The error bars represent the standard deviation of six regions-of-interest. **b,** PA signal of PDA clusters induced by different Ca^{2+} concentrations (from 0 to 200 mM). The error bars represent the standard deviation of six regions of interest. **c,** UV-vis spectra of PDA clusters at different Ca^{2+} concentration. M-NTA image shows higher light scattering (*i.e.,* brighter) of PDA clusters (200 mM) than individual PDAs (0 mM). The intensity of the blue dots is proportional to light scattering. **d,** Reversible PA signal upon assembly-disassembly of PDA clusters. PA signal turned “on and off” under repeatedly adding EDTA and Ca^{2+} ions. **e,** PA signal of PDA mixtures at the same total number of particles. 0:1, 1:4, 1:2, 1:1, 2:1, and 1:0 indicate the particle number ratio of PDA_{300} to PDA_{120}. **f,** Particle distributions of PDA mixtures at different Ca^{2+} concentrations. **g,** 3D bioprinting process of skin-tone phantom. The photograph shows the same skin phototype (Fitz. 6) of three-printed phantoms. **h,** PA signal of 3D-bioprinted phantoms containing PDA mixtures with 0, 20, and 200 mM of Ca^{2+} ions. PA signal increased as more PDA clusters led to PA punctuate images. **i**, CIE coordinates of 3D-printed phantoms containing different amounts of PDA clusters. The experiments in **a**, **b**, **d**, and **h** were repeated independently three times with similar results.

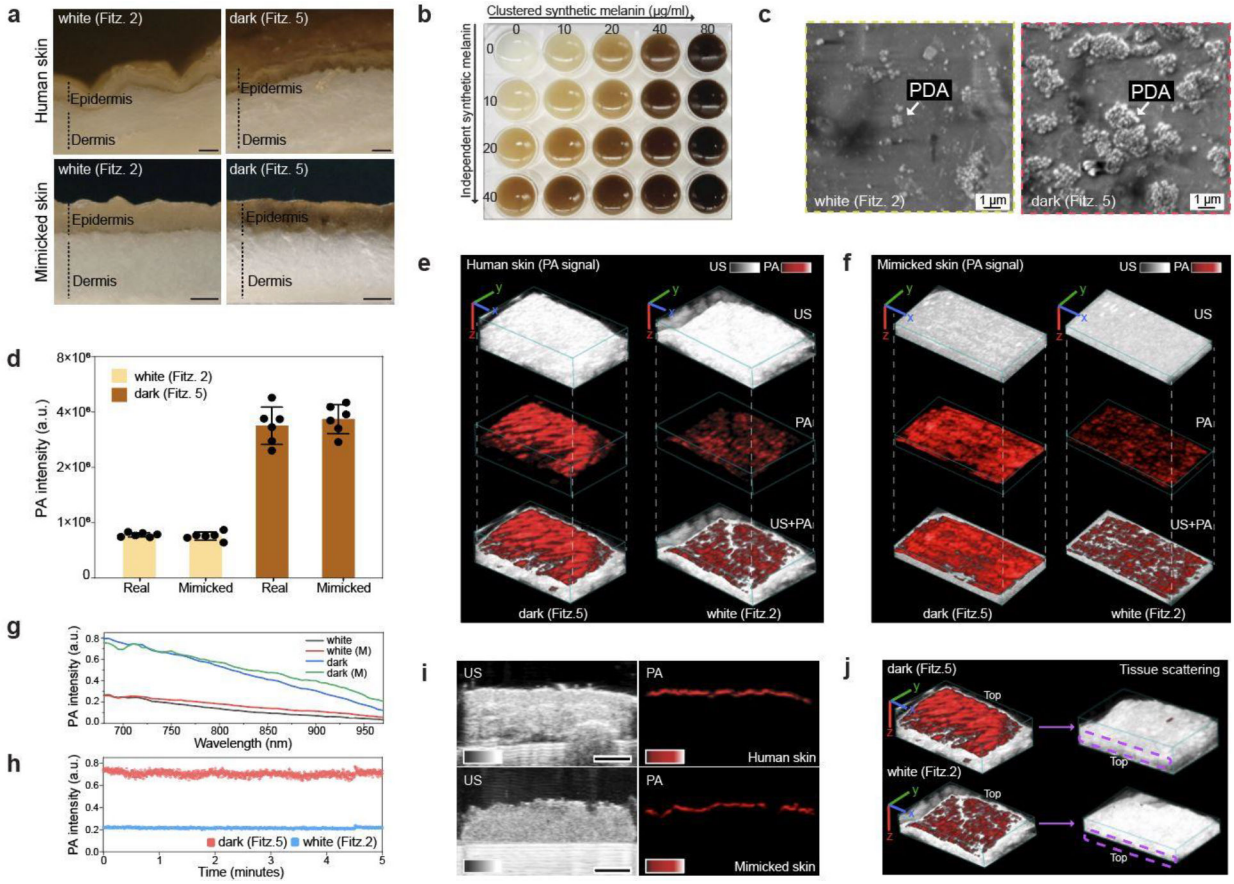

Figure 4. PA comparison between real and mimicked skin.

a, Optical images (cross-section) of real and mimicked skins. The scale bars represent 0.5 mm. **b,** Skin phototype variations. Skin colors were readily tunable (From Fitz. 1 to Fitz. 6) by adjusting PDA contents. **c,** SEM image of PDA mixtures in the printed skin (epidermal layer). **d,** PA signal comparison between real and mimicked skins. PA signal of mimicked skin was comparable to that of real human skin at the same skin phototype. The error bars represent the standard deviation of six regions of interest. PA and US image of real (**e**) and mimicked (**f**) human skins, showing randomly distributed melanosomes in epidermis. The scale bars (x, y, z) represent 4 mm. **g,** Spectral PA signal from 680 nm to 970 nm of real and mimicked (M) skins. **h,** PA signal stability of mimicked skins. **i,** PA signal of epidermis in real and mimicked skins. The scale bar represents 4 mm. **j,** Tissue scattering in real human skins. Purple dotted area indicates the region of epidermis after turning the samples upside-down. The scale bars (x, y, z) represent 4 mm. The thicknesses of dermal tissue were 4 mm (Fitz. 5) and 2.7 mm (Fitz. 2). The experiments in **g, i,** and **j** were repeated independently three times with similar results.

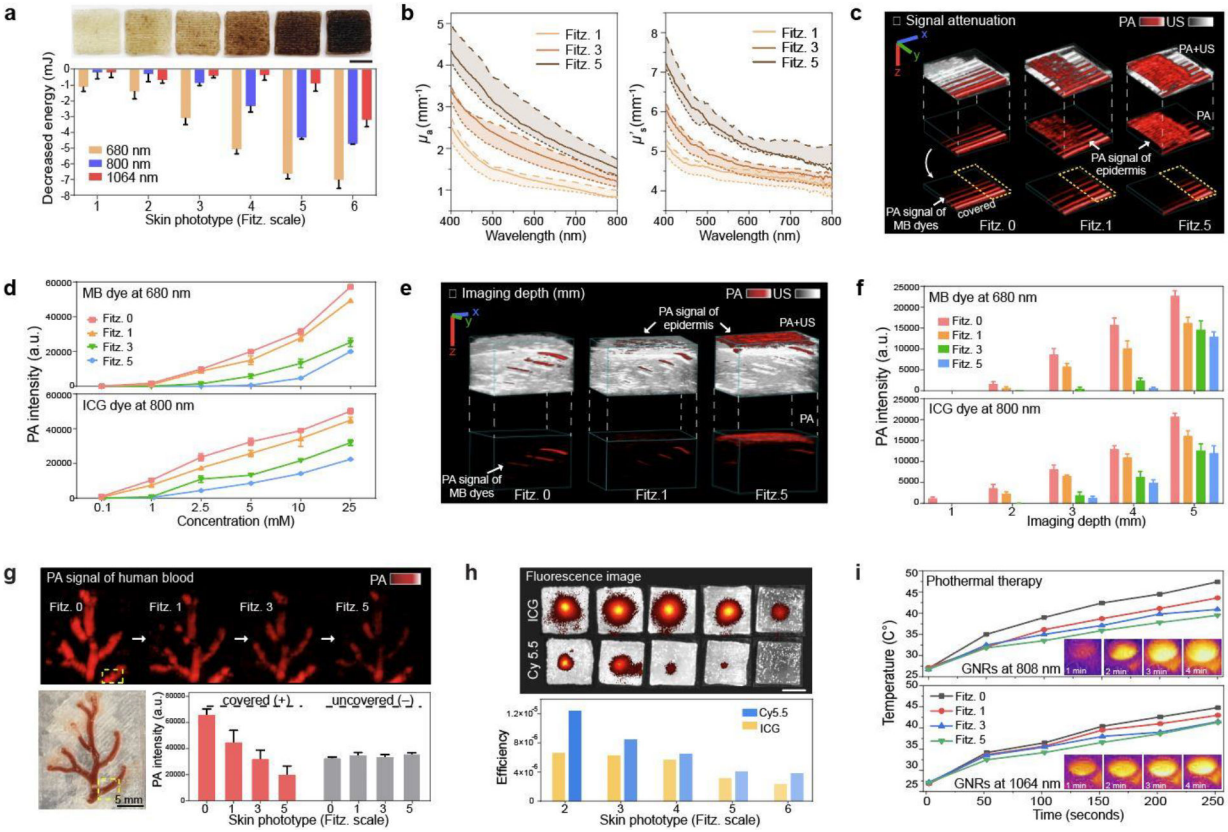

Figure 5. Impact of skin phototypes on biomedical optics.

a, Decreased energy of 680 nm, 800 nm, and 1064 nm lasers due to light absorption by mimicked skin phototypes. The error bars represent the standard deviation of three individual samples. Photograph shows 3D-bioprinted skin phantoms with different skin phototypes (from Fitz. 1 to 6). **b,** μ_a and μ_s' (solid lines) values of Fitz. 1, 3, and 5 skin phantoms. The dotted lines represent the tunable range of μ_a and μ_s' by adjusting PDA content in the epidermis. **c,** PA image of MB dye covered by Fitz. 1, 3, and 5 skin phantoms. Yellow dotted area remained uncovered showing no decrease in the laser power. The scale bars (x, y, z) represent 4 mm. **d,** PA signal attenuation of MB and ICG dyes by Fitz. 1, 3, and 5 skin phantoms. The error bars represent the standard deviation of six regions of interests. **e,** PA image of MB dye in a 5-mm-thick phantom covered by Fitz. 1, 3, and 5 skin phantoms. The scale bars (x, y, z) represent 4 mm. **f**, PA signal attenuation of MB and ICG dyes at different imaging depths from 1 to 5 mm. MB and ICG dyes (10 mM) were covered by Fitz. 1, 3, and 5 skin phantoms. The error bars represent the standard deviation of six regions of interest. **g,** PA signal attenuation of real human blood. Human blood in the blood vessel scaffold was covered by Fitz. 1, 3, and 5 skin phantoms. Yellow-dotted area remained uncovered as a negative control. The error bar represents the standard deviation of six regions of interest. **h,** Fluorescence attenuation of Cy5.5 and ICG dye by mimicked skin phototypes. Insert images show that Cy5.5 and ICG dyes were covered by phantoms with different skin phototypes from Fitz. 2 (left) to the Fitz. 5 (right). The scar bar represents 5 mm. **i,** Impact of skin phototypes on photothermal therapy. NIR-I (808 nm) and NIR-II (1064 nm) lasers were used for the test. Fitz. 0 indicates the phantom without synthetic

melanin. The experiments in **a, d, f, g, h,** and **i** were repeated independently three times with similar results.